High sensitivity multitasking non-reciprocity sensor using the photonic spin Hall effect

Jun-Yang Sui,[1] Si-yuan Liao,[1] BingXiang Li,[1,2,†] ⓘ and Hai-Feng Zhang[1,†]*

[1]*College of Electronic and Optical Engineering & College of Flexible Electronics (Future Technology), Nanjing University of Posts and Telecommunications, Nanjing 210023, China*
[2]*e-mail: bxli@njupt.edu.cn*
Corresponding author: hanlor@163.com
[†]*These authors contributed equally to this Letter.*

A non-reciprocity sensor based on a layered structure with multitasking is proposed, which realizes biological detection and angle sensing. Through an asymmetrical arrangement of different dielectrics, the sensor obtains non-reciprocity on the forward and backward scales, thus achieving multi-scale sensing in different measurement ranges. The structure sets the analysis layer. Injecting the analyte into the analysis layers by locating the peak value of the photonic spin Hall effect (PSHE) displacement, cancer cells can accurately be distinguished from normal cells via refractive index (RI) detection on the forward scale. The measurement range is 1.569~1.662, and the sensitivity (S) is 2.97×10^{-2} m/RIU. On the backward scale, the sensor is able to detect glucose solution with 0~400 g/L concentrations (RI = 1.3323~1.38), with $S = 1.16 \times 10^{-3}$ m/RIU. When the analysis layers are filled with air, high-precision angle sensing can be achieved in the terahertz range by locating the incident angle of the PSHE displacement peak; 30°~45°, and 50°~65° are the detection ranges, and the highest S can reach 0.032 THz/°. This sensor contributes to detecting cancer cells and biomedical blood glucose and offers a new way to the angle sensing.　© 2022 Optica Publishing Group

The photonic spin Hall effect (PSHE) [1] refers to the fact that during total reflection, affected by conservation of spin and orbital angular momentum, two beams will be generated by the left-handed and right-handed circular polarization components of linearly polarized light splitting in opposite transverse directions perpendicular to the refractive index (RI) gradient, depending on the direction of rotation. Because the spin offset in PSHE is very sensitive to changes in the physical parameters of the system, it has great application potential in precision measurements [2]. Fortunately, Hosten and Kwiat [3] used a weak measurement technique to amplify the PSHE phenomenon observed in the experiment. Graphene is one of the most widely studied materials with excellent properties. Recently, Dong *et al.* [4] discovered that graphene monolayers introduced into silica aerogel layers can significantly enhance the PSHE. Moreover, some scholars have proposed using the tunable chemical potential of graphene to effectively enhance and regulate the PSHE

[5]. Ideas are given by these findings for improving the PSHE in the terahertz (THz) range.

Abnormal blood sugar can lead to hyperglycemia, glucose being the prime component of blood sugar [6], and precise detection of the concentration is important to keep food safe and guard human health [7]. Studies have shown that before the invasion of cancer cells, the nucleus becomes larger in volume and the RI is higher than that of normal cells due to increased chromatin [8]. Therefore, the RI of cells may become an indicator of early cancer cells. The RI sensors based on the PSHE are considered a promising diagnostic tool with high sensitivity (S), no labeling, and supervision. In recent years, Zhou *et al.* [9] established a theoretical model between the PSHE and the optical isomer composition ratio in geometric optical images, obtaining the concentration of glucose and fructose in the mixed solution with a precision up to 0.0096 g/L and 0.0172 g/L, respectively. Dong *et al.* [10] enhanced the PSHE by light pumping and achieved RI sensing in the THz range, enabling distinction between normal cells and cancer cells at the same concentration. Although the above sensors based on the PSHE have excellent sensing performance, their sensing function is single and not multi-scale. Badri and Farkoush [11], based on a sub-wavelength grating, devised a reconfigurable optical band-pass filter that not only could adjust the resonant wavelength and transmission peak but also act as a non-volatile optical switch, providing new ideas for research.

Multitasking PSHE sensors suitable for a variety of application scenarios have widespread research prospects. For example, the rotation angle measurement of a bridge support is an important standard to evaluate the bridge state. The expected maximum rotation angle of an ordinary bridge with a span of 30 m is only about 0.01°, but existing tiltmeters do not have sufficient resolution and precision to measure weak angle changes [12]. Likewise, module docking is one of the key factors affecting the overall quality of spacecraft and it is important to realize the docking by providing adjustment technology with high-precision angle measurement [13]. A system utilizing cameras and image processing techniques has been developed to measure weak angle changes [14], although this system is easily affected by external environmental changes and needs very complex equipment. Therefore, high-precision angle measuring devices with the attributes

Table 1.   Non-Reciprocal Performance of the Sensor

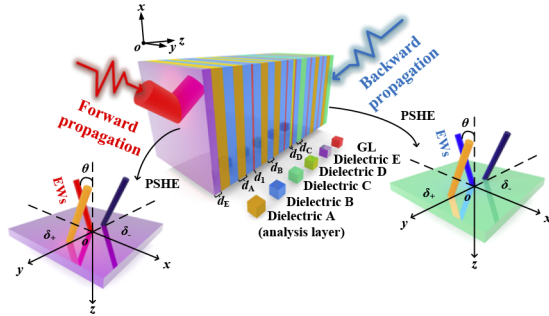|		Biosensing	Angle Detecting
Forward	**Range**	1.659~1.662	30°~45°
	S	2.97×10^{-2} m/RIU	0.032 THz/°
Backward	**Range**	1.3323~1.38	50°~65°
	S	1.07×10^{-3} m/RIU	0.026 THz/°

Fig. 1. Schematics of the layered structure. The entire structure is E(ABABGLB)²DGLBC(BGLBA)²C. The thicknesses of the mediums A, B, C, D, E, and the GL are $d_A = 15$ µm, $d_B = 15$ µm, $d_C = 20$ µm, $d_D = 3$ µm, $d_E = 7.5$ µm, and $d_1 = 0.34$ nm, respectively.

of simplicity, stability, and multi-scene applicability are needed.

In this Letter, a non-reciprocity sensor with multitasking based on a layered structure is proposed, which offers both biological and angle detection. Based on an appropriate asymmetric structure, the non-reciprocity is enhanced, equipping the sensor with two detection scales (the details have been indicated in Table 1). In addition, an analysis layer is left for RI sensing of the analyte. By introducing a graphene layer (GL) and selecting a suitable chemical potential μ_C, the PSHE is strengthened. When performing biosensing, the analyte is infused into the analysis layer. By RI detection, normal stomach, liver, and epidermal cells and their corresponding cancer cells can be distinguished on the forward scale. On the backward scale, the sensor can detect the concentration of aqueous glucose solution (C_G) with a range of 0~400 g/L. The highly sensitive biosensing with different RI detection ranges is the highlight of this paper. The layered structure means that the sensor can achieve angle detection with high precision when there is no analyte in the analysis layer, that is when it is filled with air. The angle detection sensor based on a layered structure has the advantages of a compact structure, small size, and convenient portability. Moreover, due to the use of THz-band electromagnetic waves (EWs) for angle detection compared with infrared radiation, it is less affected by the harsh environment. This novel multitasking and multi-scale sensor based on the PSHE is a complement to the traditional single-function sensor, offering research prospects in a variety of scenarios and physical quantities.

The proposed layered structure is exhibited in Fig. 1, which is formed by an asymmetric quasi-periodic arrangement of ordinary dielectrics and a GL filled with different colors. To adapt to ordinary conditions, the layered structure is exposed to air and the selected operating temperature T is 270 K. The cases where the EWs propagate from the front and back are respectively indicated by red and blue colors. The dielectric A is set as the analysis layer. When biosensing is applied to distinguish cancer cells from normal ones and detect C_G, by injecting the analyte

into the analysis layer for RI sensing with a precise technique based on micro-infiltration technology by hollow submicron size pipettes [15], the RI of dielectric A (n_A) will change accordingly. The RI of the other dielectrics is $n_B = 2$, $n_C = 3$, $n_D = 5$, and $n_E = 2$. It should be emphasized that Leiwin [16] derived effective permittivity and permeability expressions for composites based on Mie resonance theory, and the desired RI can be obtained over a wide range. This technology has been applied in practice [17], so the permittivity set in this paper is reasonable and can be obtained in reality. For the fabrication of layered structures, the etching method outlined by Guo *et al.* in Ref. [18] can be used (see Supplement 1 Part 1). Because theoretical investigation is the key to such a paper, the experimental verification is out of the scope of this article. The surface conductivity σ belonging to the GL is composed of the intraband σ_{intra} and interband σ_{inter}, and the dielectric function of the GL can be found (details can be seen in Supplement 1 Part 2).

Figure 1 also indicates the setting of a Gaussian beam with a certain incident angle θ to present the PSHE phenomenon. Here, orange and dark blue beams, respectively, represent the components of the left-handed and right-handed circular polarization reflected at the interface. H and V are utilized to symbolize horizontal and vertical polarization. For simplicity, vertical polarization is not considered. For horizontal polarization reflected light, the PSHE lateral displacements of the components belonging to left-handed and right-handed circular polarization are symbolized by δ^H_+ and δ^H_- respectively (see Supplement 1 Part 3):

$$\delta^H_\pm = \mp \frac{\lambda}{2\pi}[1 + \frac{|r^s|}{|r^p|}\cos(\varphi^s - \varphi^p)]\cot\theta_i, \tag{1}$$

$$\delta^V_\pm = \mp \frac{\lambda}{2\pi}[1 + \frac{|r^p|}{|r^s|}\cos(\varphi^p - \varphi^s)]\cot\theta_i. \tag{2}$$

In this paper, only the case of right-handed circularly polarized component displacement δ^H_- is discussed.

μ_C indicates the externally controllable chemical potential of the GL by modulating the external voltage. The way to change the GL μ_C experimentally is outlined by Qi *et al.* in Ref. [19] (see Supplement 1 Part 4 for details). To explain the generation of the peak of δ^H_- and the choice of μ_C, setting the RI of the analysis layer as 1.659 means the EWs are incident from the front at 3.6 THz. Here, μ_C takes four standard values of 0.1 eV, 0.3 eV, 0.5 eV, and 0.7 eV. Figure 2 indicates the relationship between the absolute values $|r^s|$ and $|r^p|$ of Fresnel coefficients and the incidence angle at different μ_C. The solid red and dashed blue lines represent the reflection coefficient curves of $|r^s|$ and $|r^p|$, respectively. The change of μ_C will affect the σ, thus altering the Fresnel coefficients and regulating δ^H_- [6]. Additionally, due to the introduction of the defect layer, the energy is localized and the reflection gap is generated where $|r^s|$ and $|r^p|$ drop rapidly, forming defect peaks. The reflection gap is generated at different angles under diverse μ_C. As can be seen from Figs. 2(a)–2(d), as the μ_C increases, the θ corresponding to the curve peaks of $|r^s|$ and $|r^p|$ gradually become smaller. When $\mu_C = 0.3$ eV, the peak value of $|r^p|$ reaches the minimum at 38.99°, where the defect peak generates ($|r^p|$=0.02). By the beam displacement of Eqs. (1) and (2), the division of the spin correlation mainly depends on the part of $|r^s|/|r^p|$, so the $|r^s|/|r^p|$ can reach a large value near the defect peak of $|r^p|$, resulting in the peak of δ^H_-. This theory is tested in Fig. 3. Figure 3(a) shows the δ^H_- values under different μ_C, and as μ_C increases, the peaks of δ^H_- gradually
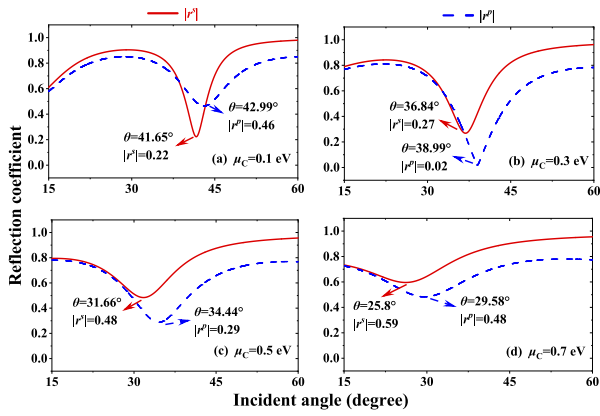
Fig. 2. Reflection coefficient curves of $|r^s|$ and $|r^p|$ with different μ_C: (a) $\mu_C = 0.1$ eV, (b) $\mu_C = 0.3$ eV, (c) $\mu_C = 0.5$ eV, and (d) $\mu_C = 0.7$ eV.
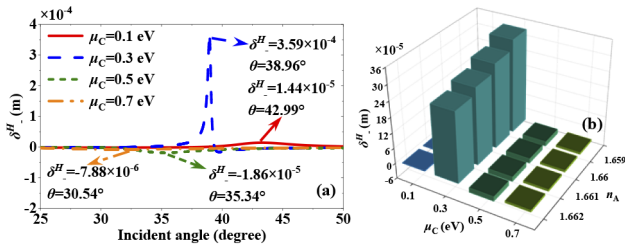

Fig. 3. When μ_C changes and EWs are incident from the front: (a) comparison plots of δ^H_- under $n_A = 1.659$, and (b) plots of δ^H_- peak values under different n_A.

Table 2. Three Types of Normal Cells and Cancer Cells and Their RI at the Same Concentration [8]

	Type	Density (cells/mL)	RI Value (RIU)
Normal	GES-1	4.48×10^5	1.65998
	LO2	4.48×10^5	1.66013
	HEM	4.48×10^5	1.66034
Cancer	MGC-803	4.48×10^5	1.66104
	7721	4.48×10^5	1.66069
	MEL	4.48×10^5	1.66124

move to a small angle. δ^H_- produces the highest peak at 38.96°, $\delta^H_- = 3.59 \times 10^{-4}$ m when $\mu_C = 0.3$ eV. δ^H_- peaks at μ_C of 0.1 eV, 0.5 eV, and 0.7 eV are small, the values being 1.44×10^{-5} m, -1.86×10^{-5} m, and -7.88×10^{-6} m belonging to θ of 42.99°, 35.34°, and 30.54°, respectively. To more accurately select the appropriate μ_C, Fig. 3(b) indicates the changing pattern of the δ^H_- peak values corresponding to different μ_C within the n_A range of 1.659~1.662. The peak value of δ^H_- corresponding to $\mu_C = 0.3$ eV is significantly larger than the values of δ^H_- under other values of μ_C and varies significantly with the size of RI. Because the RI detection of biosensing is achieved by locking the δ^H_- peak, the selection of $\mu_C = 0.3$ eV leads to excellent sensing performance.

Table 2 shows three types of human normal cells and their corresponding cancer ones [8]: normal stomach cells (GES-1), normal liver cells (LO2), normal epidermal cells (HEM); and gastric cancer cells (MGC-803), liver cancer cells (7721), epidermal cancer cells (MEL). At the same concentration of
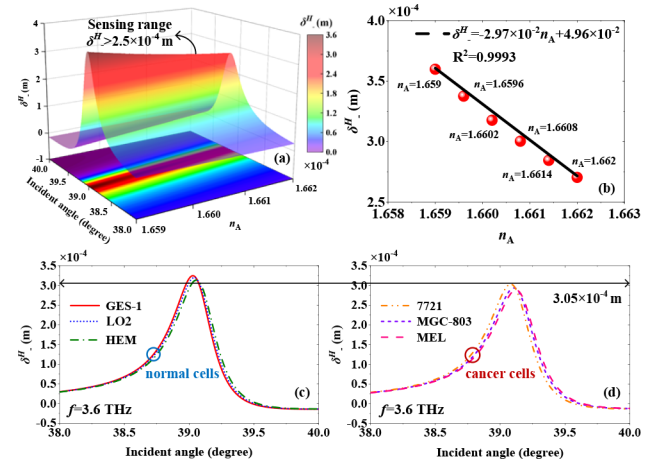

Fig. 4. Schematic diagrams of the RI sensing when EWs propagate forward: (a) continuous varying δ^H_- peaks, (b) LFR between n_A and δ^H_-, (c) δ^H_- peaks belonging to normal cells, and (d) δ^H_- peaks belonging to cancer cells.

4.48×10^5 cells/mL, compared to normal ones, cancer cells generally have a higher RI because their larger nuclei contain more proteins to facilitate rapid cell division. Hence, RI is an important identification indicator [8]. Next, the PSHE sensor is applied to distinguish the cancer cells from normal ones with high precision which can respond sensitively to the change of 1×10^{-5} RIU.

Similar to the principle of δ^H_- change caused by μ_C, RI modulation will influence the tweaks of wave vector and phase, which in turn affects the size of Fresnel reflection coefficients $|r^s|$ and $|r^p|$. Hence, both δ^H_- and θ corresponding to the peak vary accordingly. By locking the δ^H_- peak values, RI sensing can be realized. When the $n_A = 1.659~1.662$ as EWs propagating forward at 3.6 THz, Fig. 4(a) indicates that the peak values of δ^H_- in the 38°~40° angle range display significantly continuous variation. Peak values decrease gradually but at least exceed 2.5×10^{-5} m, which ensures basic detectability. The linear fitting relationship (LFR) is obtained by selecting equidistant points along the horizontal axis and using the linear fitting method. Figure 4(b) exhibits the LFR between n_A and δ^H_-. In the RI range of 1.659~1.662, the LFR is $\delta^H_- = -2.97 \times 10^{-2} n_A + 4.96 \times 10^{-2}$. R^2 is applied to evaluate the quality of linear fit. $R^2 = 0.9993$ proves that the sensor is reliable. S can reach 2.97×10^{-2} m/RIU. The RI detection range of 1.659~1.662 completely covered the RI belonging to solutions of normal cells and cancer ones at the same concentration (4.48×10^5 cells/mL) [8]. To observe the difference between normal and cancer cells directly, Figs. 4(c) and 4(d) respectively show the δ^H_- curves belong to three types of normal cells and the corresponding cancer ones. Compared with normal cells, the δ^H_- peak values belonging to cancer cells in Table 2 are smaller (Supplement 1 Part 5 indicates a clearer comparison). Additionally, Figs. 4(c) and 4(d) also offer a simple and rapid method to identify cancer cells: at 4.48×10^5 cells/mL concentration, when the maximum δ^H_- value is lower than 3.05×10^{-4} m, it can be judged as a cancer cell solution. Compared with the RI sensor using the local resonance optical tunneling effect to detect cancer cells with S = 24.8 μm/RIU [8], the designed sensor has excellent sensing performance.

The layered structure can be applied to detect the C_G when EWs propagate from the back direction at 2.3 THz. Since the C_G has an RI close to the blood glucose concentration, the study on
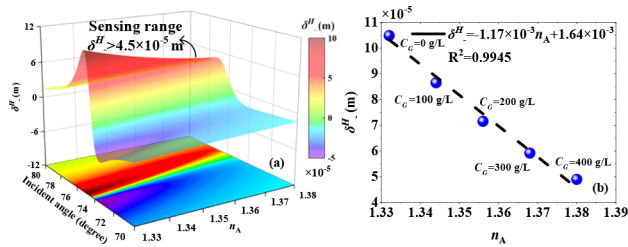
Fig. 5. Schematic diagrams of the RI sensing when EWs propagate backward: (a) continuous varying δ^H_- peaks, (b) LFR between n_A and δ^H_-.
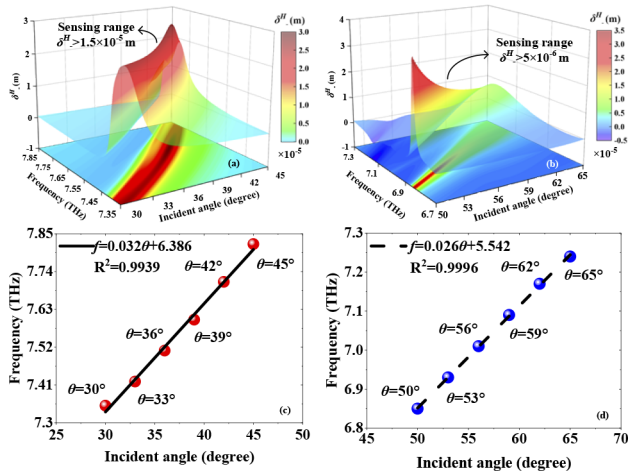

Fig. 6. Schematic diagrams of the incident angle sensing. Continuous varying δ^H_- peaks: (a) when EWs propagate forward, and (b) when EWs propagate backward. LFR between the incident angle and frequency: (c) on the forward scale, and (d) on the backward scale.

the former is able to provide a certain basis for the latter. The C_G is infused into the analysis layer and the relationship between the RI and C_G can be expressed as [20]:

$$nA = 1.33230545 + 0.00011889C_G. \tag{3}$$

In Fig. 5(a), within the θ range of 70°~80°, δ^H_- peak values decrease gradually as the n_A increases from 1.3323 to 1.38 (C_G varies from 0~400 g/L), and $\delta^H_- > 4.5 \times 10^{-5}$ m in the sensing range. With the increase of n_A, the peak value of δ^H_- decreases and moves in the direction of larger θ. Figure 5(b) indicates the LFR between C_G and δ^H_- peak value. If C_G increases from 0 g/L to 400 g/L in 100 g/L intervals, in the 1.3323~1.38 RI measured range, $\delta^H_- = -1.17 \times 10^{-3} n_A + 1.64 \times 10^{-3}$ is the LFR (the displacement δ^H_- of each detection point is shown in Supplement 1 Part 6). R^2 reaches 0.9945, reflecting low measurement error and high linearity reliability. S = 1.17×10^{-3} m/RIU, which indicates highly sensitive detection, raising a new possibility to subtly observe blood glucose concentration.

It is also found that when there is no analyte in the analysis layer—that is it is filled with air ($n_A = 1$)—the incident angle θ corresponding to the δ^H_- will move regularly with the variation of the frequency f of the incident EWs, which can be used as a mean to detect the angle of EWs. On the forward and backward scales, Figs. 6(a) and 6(b) show good linear relationships between θ and f via the δ^H_- peak. When θ increases in the range of 30°~45° forward and 50°~65°

backward, the δ^H_- peak produces blueshift. However, their δ^H_- peaks are respectively larger than 1.5×10^{-5} m and 5×10^{-6} m, ensuring basic detectability. To explore their linear relationship, the correlative LFRs $f = 0.032\theta + 6.386$ and $f = 0.026\theta + 5.542$ are presented in Figs. 6(c) and 6(d). 0.032 THz/° and 0.026 THz/° are the corresponding values of S. Corresponding values of R^2 are 0.9939 and 0.9996, indicating the high quality of the linear fit. The above research indicates that the sensor offers multiple different θ detection ranges, and the LFRs of detection are excellent, meaning a sensitive response. It provides a novel and stable way to detect weak θ change in the THz band.

In summary, a multi-scale and multitasking sensor is proposed. It has forward and backward scales, and can precisely measure different ranges of RI and θ. The sensing properties of the layered structure are studied. When the sensor is used for biosensing via the peak values of δ^H_-, the related RI detection range can reach 1.659~1.662 forward and 1.3323~1.38 backward (S = 2.97×10^{-2} m/RIU and 1.17×10^{-3} m/RIU, respectively). When used for incident angle measurement, the analysis layer is filled with air. By locking the θ of the δ^H_- peak, θ sensing can be realized in the range of 30°~45° forward and 50°~65° backward with the corresponding values of S being 0.032 THz/° and 0.026 THz/°. This sensor with a compact structure and excellent performance has powerful application prospects.

Disclosures. The authors declare no conflicts of interest.

Data availability. Data underlying the results presented in this paper are not publicly available at this time but may be obtained from the authors upon reasonable request.

Supplemental document. See Supplement 1 for supporting content.

REFERENCES

1. A. Kavokin, G. Malpuech, and M. Glazov, Phys. Rev. Lett. **95**, 136601 (2005).
2. X. Zhou, X. Ling, and H. Luo, Appl. Phys. Lett. **101**, 251602 (2012).
3. O. Hosten and P. Kwiat, Science **319**, 787 (2008).
4. P. Dong, J. Cheng, and H. Da, Opt. Commun. **485**, 126744 (2021).
5. X. Bai, L. Tang, and W. Lu, Opt. Lett. **42**, 4087 (2017).
6. F. Amiripour, S. Ghasemi, and S. N. Azizi, Appl. Surf. Sci. **537**, 147827 (2021).
7. Z. Vafapour, IEEE Trans. on Nanobioscience **18**, 622 (2019).
8. A. Jian, M. Jiao, and Y. Zhang, Sens. Actuators A: Physical **313**, 112177 (2020).
9. H. Zhou, Y. Wei, and W. Hao, Appl. Opt. **56**, 5794 (2017).
10. P. Dong, J. Cheng, and H. Da, New J. Phys. **22**, 113007 (2020).
11. S. H. Badri and S. G. Farkoush, Appl. Opt. **60**, 2803 (2021).
12. Y. S. Park, J. A. Agbayani, and J. H. Lee, J. Sensors **2015**, 1 (2015).
13. L. Yuan, F. Yunfeng, and S. Yinhao, Journal of Ordnance Equipment Engineering. **39**, 8 (2018).
14. H. Jeon, Y. Bang, and H. Myung, Smart Mater. Struct. **20**, 045019 (2011).
15. F. Intonti, S. Vignolini, and V. Turck, Appl. Phys. Lett. **89**, 211117 (2006).
16. L. Lewin, J. Inst. Elect. Eng.-Part III: Radio Commun. Eng. **94**, 65 (1947).
17. X. Liu, Z. Qian, and C. Lan, Appl. Phys. Lett. **103**, 031910 (2013).
18. S. Guo, C. Hu, and H. Zhang, J. Opt. **22**, 105101 (2020).
19. L. Qi, C. Liu, and S. M. A. Shah, Carbon **153**, 179 (2019).
20. S. Ghorbani, M. Sadeghi, and Z. Adelpour, Laser Phys. **30**, 026204 (2020).